JM PAPERS

Sub-surface turbulence or non-breaking capillary waves: which dominates air–water gas transfer?

Leon Li[1] , Pim A. Bullee[1,2] , Simen Å. Ellingsen[1] and R. Jason Hearst[1]

[1]Department of Energy and Process Engineering, NTNU, Kolbjørn Hejes Vei 2, 7491 Trondheim, Norway
[2]Institute of Fluid Dynamics, ETH Zürich, Sonneggstrasse 3, 8092 Zürich, Switzerland
Corresponding author: R. Jason Hearst, jason.hearst@ntnu.no

We examine the separate effects of turbulence beneath a free surface and non–breaking surface capillary waves on the gas-transfer velocity of atmospheric oxygen into water across an air–water interface. The experiments are conducted in a recirculating open water channel with quiescent air, where atmospheric oxygen naturally dissolves into the water via the exposed surface. Through the combination of an active turbulence grid and an array of surface penetrating dowels, we are able to separate the effects of sub-surface turbulence and surface capillary waves. The findings demonstrate that the gas-transfer velocity trends with the turbulence properties, not the capillary wave properties, thus indicating that, when both are present, it is the sub-surface turbulence, not the capillary waves, that plays the dominant role in determining the rate of gas transfer across an air–water interface in the non-breaking capillary wave regime.

Key words: wave–turbulence interactions, capillary waves

1. Introduction

The concentration of essential gas species in the global hydrosphere, such as O_2 and CO_2, plays a role in the Earth's climate and biosphere that cannot be overstated. An accurate understanding of oceanic carbon sequestration processes is paramount for reliable climate predictions. The rate at which mass, momentum and temperature are exchanged between the atmosphere and open waters, for instance at the ocean surface, depends on a plethora of factors. These factors are extensively summarised by Garbe *et al.* (2014) and Deike (2022), and include, but are not limited to, small- and large-scale turbulence, wind induced capillary-gravity waves, bubble entrainment, salinity and surfactants. These make for a system of high complexity with processes that are manifold and interlinked.

Many – but far from all – of the physical processes that affect gas exchange are caused by wind, either directly or indirectly, hence the most-used models in large simulations express gas transfer as a function of wind speed only; it is common to employ either the reference wind speed at 10 m, U_{10}, or the friction velocity on the water surface, u^*, cf. Wanninkhof *et al.* (2009), Garbe *et al.* (2014) and Deike (2022). For cases where there are no breaking waves, changes to the gas transfer have been mainly attributed to either the wind-induced surface ripples (Bock *et al.* 1999) or sub-surface turbulence (e.g. Zappa *et al.* 2007). Field studies in the presence of wind have found the rate of gas transfer to correlate well with the mean-square slope of the surface (Frew *et al.* 2004) or water-side turbulence parameters, e.g. friction velocity (Esters *et al.* 2017) or dissipation (Zappa *et al.* 2007). These seemingly independently support views that either the surface topology or the water turbulence is the driving mechanism. Yet, in these field studies, both the ripples and the turbulence are generated by the same mechanism (wind stress) and are thus inherently linked.

By studying gas-transfer rates in a well-controlled environment where the effects of turbulence are isolated from capillary waves and *vice versa*, we aim to contribute to the knowledge of their individual effects on the gas-transfer rate, k. In a recent extensive sensitivity study by Woolf *et al.* (2019), variations in the values of k for the transfer of atmospheric CO_2 into water led to the largest contribution to the overall variations in the estimated net global CO_2 air–sea flux, overshadowing other factors such as geographical and temporal differences in sampling, thermal gradient variations and salinity gradient variations. Furthermore, gas evasion from the global river system is similar in magnitude to the total gas sequestration by the oceans (e.g. Horgby *et al.* 2019), and the sub-surface turbulence found in river flows is not usually wind made and is more likely to be decoupled from the atmospheric conditions. Thus, separating the effects of turbulence and waves has applicability beyond the ocean carbon sequestration process. In the present study, we specifically aim to disconnect surface ripples from turbulence in order to discern whether it is non-breaking capillary waves or sub-surface turbulence that governs the gas-transfer process.

The mass flux through an air–water interface, F, can be modelled as the product of the concentration difference and the gas-transfer velocity, k (typically reported in units of cm h^{-1}), *viz.*

$$F = k(C_s - C_b). \tag{1.1}$$

Here, C_s is the saturated gas concentration in the water, and C_b is the gas concentration within the water, away from the interface. Hence, for undersaturated water ($C_b < C_s$) a gas flux across the air–water interface will develop until either saturation or equilibrium is reached. That the fluid mechanics in the water phase would impact k at all requires that the fluidic diffusivity significantly outweighs the mass diffusivity of the particular species. For CO_2 transport across a flat air–water interface into a turbulent flow, Variano & Cowen (2013) showed that the eddy diffusivity is five orders of magnitude greater than the mass diffusivity. Moreover, the Schmidt number, $Sc = \nu/D$ where ν is the kinematic viscosity and D is the mass diffusivity, for O_2 and CO_2 are in the range $450 \lesssim Sc \lesssim 700$, also indicating that, once the species is in the water, viscous diffusivity dominates over mass diffusivity (Wanninkhof *et al.* 2009).

It is worth noting that the solubilities of O_2 and CO_2 are almost an order of magnitude different, and as a result, the roles of wave breaking and bubbles in their transport are quite different (e.g. Garbe *et al.* 2014; Deike 2022). Nonetheless, in conditions where such phenomena do not dominate the process, i.e. when the interface is flat or when there are non-breaking capillary waves, interfacial transport of these gases is considered to be dominated by the fluid side of the interface (Herlina & Jirka 2008; Garbe *et al.* 2014). In such cases, two prominent models for k are the thin-film model (Nernst 1904) and

the surface renewal model (Danckwerts 1951). In the former, gas exchange from air to water is controlled by the process of molecular diffusion through a thin film at the liquid surface. For gases with low solubility, this process is often the bottleneck in the mass flux process and can wholly control the value of k. The surface renewal model, on the other hand, posits that k is determined by the rate at which parcels of fresh, unsaturated bulk fluid are transported to the surface by the sub-surface flow, where they can rapidly absorb gas species from the air, before being replaced by new fluid parcels. For flows with a significant degree of bulk turbulence in either phase, Danckwerts (1951) argues that turbulence is the dominant mechanism for k, and Lamont & Scott (1970) suggested a parameterisation in terms of viscous dissipation. The thin-film and surface renewal models are not necessarily mutually exclusive, and efforts have been made to combine the two, explaining the increase in k as caused by distortions to the thin film through near-surface turbulence (e.g. MacIntyre 1971; Longuet-Higgins 1992; Szeri 1997).

Several experimental studies have been performed to test these hypotheses with varying results (Kanwisher 1963a,b; Liss 1973; Henstock & Hanratty 1979; McCready & Hanratty 1985; Coantic 1986; Jähne *et al.* 1987; Komori, Nagaosa & Murakami 1993; Saylor & Handler 1997; Adler & Cowen 2022). The observed increase in k differs greatly from the model prediction in some cases. For example, Saylor & Handler (1997) saw an increase in k by two orders of magnitude in the presence of waves in a shaken container (Faraday waves), much higher than MacIntyre's (1971) prediction of 3.5. Saylor & Handler (1997) also argued that their experiment isolated the effects of capillary waves as they were generated by surface excitation of a quiescent water tank. That pure surface wave motion might increase k to this degree may be surprising: the relative increase in surface area is modest (in fact, Saylor & Handler (1997) themselves dismissed this being a significant contributor to the increase in k), and the orbital wave motion alone does not entail surface renewal. On the other hand, when only bulk turbulence is present with minimal surface distortions, k also increases (Herlina & Jirka 2008; Jirka, Herlina & Niepelt 2010; Variano & Cowen 2013; Bullee *et al.* 2024). Indeed, surface imprints of sub-surface turbulent structures are closely connected to surface renewal (Kermani & Shen 2009; Babiker *et al.* 2023).

It would appear from these experiments that both the surface capillary waves and the bulk flow play important roles in controlling k. However, surface deformations and sub-surface flow often occur together, sometimes relatively decoupled, at other times the former is an imprint of the latter (Brocchini & Peregrine 2001; Savelsberg & van de Water 2009; Babiker *et al.* 2023; Aarnes *et al.* 2025). In several experiments that focused on the capillary waves (e.g. Jähne *et al.* 1987; Saylor & Handler 1997; Adler & Cowen 2022), bulk turbulence was present, but not characterised, so the evidence appears inconclusive as to whether the increase in k is caused by the capillary waves alone. It can be quite difficult to design an experiment that can separate the effects of the two (Henstock & Hanratty 1979); for instance Faraday waves are often accompanied by a sub-surface convective flow (Périnet *et al.* 2017; Colombi *et al.* 2022).

To address this conundrum, we devise a set-up where the influence of capillary waves and sub-surface turbulence can be varied independently, using an active turbulence grid and a dowel array; the latter was inspired by the novel work of Adler (2022).

2. Experimental set-up

The experiments were performed in the water channel facility at the Norwegian University of Science and Technology (NTNU). The test section is an open channel made from float glass panes supported by a stainless steel frame, providing optical access from all sides. The test section measures 11.2 m in length (x_1), and is 1.8 m by 1.0 m in cross-sectional
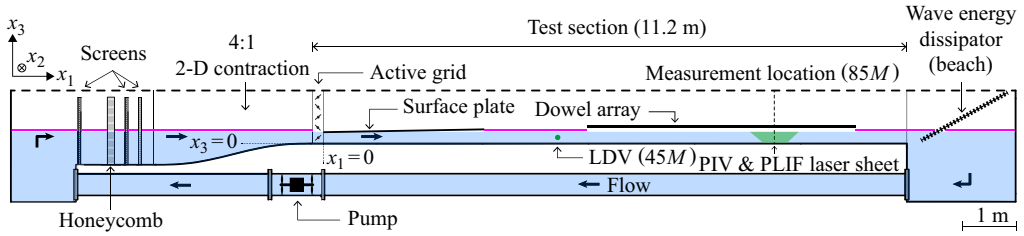
Figure 1. Scale schematic of the experimental set-up, showing the open water channel facility, the coordinate system, and the locations of the dowel array and the measurements. The purple lines represent the plastic surface coverings.

area (x_2 by x_3). The flow is driven by a pair of axial pumps, each with two counter-rotating impellers, embedded in two return pipes located below the test section. Flow conditioning is provided by three screens and a honeycomb located upstream of a 4:1 contraction. A beach is installed downstream of the test section to dissipate surface waves. Figure 1 shows a schematic of the facility.

The facility is equipped with a Makita-style (1991) active grid which has been previously used for wave–turbulence interaction (Smeltzer *et al.* 2023) and gas-transfer studies (Bullee *et al.* 2024). The active grid present in the water channel at NTNU measures 1.8 m by 1.0 m in cross-sectional area, the same as the test section, and has 28 independently controlled stepper motors spaced $M = 0.10$ m apart, each rotating a horizontal or vertical line of diamond-shaped, interlocking wings of side length M designed to perturb the inflow. A 3 m long surface plate is placed immediately downstream of the active grid to minimise the surface waves directly caused by the actuation of the wings. More details about the water channel and the active grid are available in Jooss *et al.* (2021). We used two different grid modes: 'OFF' wherein all the wings were held parallel to the mean flow direction, and 'ON' wherein all the wings were rotated in a random pattern with a frequency range of $\Omega = 0.05 \pm 0.025$ Hz to produce turbulence that was approximately homogeneous in transverse planes (Hearst & Lavoie 2015). Using this approach, we are able to produce two flows with different turbulence characteristics but near-identical bulk flow rate. To generate the surface capillary waves, an array of dowels of diameter 3.1 mm and 60 mm (150 mm) streamwise (spanwise) spacing, penetrates the water surface between $x_1 = 50M$ and $100M$. We investigated two penetration depths: 'shallow' ($\sim$7.5 mm) and 'deep' ($\sim$70 mm). The two dowel depths create similar surface capillary waves but different sub-surface turbulence generated by the dowel wakes. The active grid can mimic the sub-surface turbulence created by the dowels, but with a different surface condition compared with the regular capillary waves made by the dowels.

The combination of the active grid and the dowel array essentially gives us the ability to permutate through two different states of the bulk turbulence and capillary waves, namely 'on' or 'off'. The bulk turbulence is 'on' when the grid is ON or when the dowel array is inserted deep, while the capillary waves are 'on' when the dowel array is inserted. Including a reference case, we thus have the five different test cases listed in table 1. Here, we use an alpha-numeric naming convention for the cases, where N, S and D denote no dowels, shallow dowels and deep dowels, respectively, and 0 and 1 denote the active grid being OFF or ON, respectively. Figure 2 shows a schematic of the set-up as well as example images of the flow. We removed any bulk Reynolds number effects by keeping the water flow velocity constant at $U_\infty = 0.42$ m s^{-1} and the water depth constant at $H = 0.23$ m. Here, U_∞ is measured at a depth of $H/2$ by a laser Doppler velocimetry (LDV) probe located at $x_1/M = 45$, $5M$ upstream of the dowel array, which also provides the turbulence inflow statistics listed in table 1.

Case		N0	S0	D0	N1	S1
Grid mode		OFF	OFF	OFF	ON	ON
Dowel config.		None	Shallow	Deep	None	Shallow
u'_1/U_∞	[%]	3.2	3.2	3.3	9.0	8.8
$L_{11,\infty}/H$		0.05	0.06	0.06	1.01	1.01
Sc		508	498	487	508	500
Re_T		2170	2610	3500	25050	24990
Re_λ		156	175	237	427	411
We		0.31	0.38	0.68	5.40	5.45
h'	[mm]	0.15	0.42	0.42	0.18	0.55
$\overline{S^2}_{PLIF}$	[$\times 10^{-2}$]	0.53	8.70	10.00	0.67	9.03
$\overline{S^2}_{model}$	[$\times 10^{-2}$]	1.06	13.28	15.27	1.34	13.78
$\Delta\mathcal{A}$	[%]	0.53	6.64	7.64	0.67	6.89
u'_{1b}/U_∞	[%]	4.48	4.68	6.30	6.83	6.96
L_{11}/H		0.27	0.30	0.30	2.01	1.95
k	[cm h^{-1}]	31.2	34.7	42.1	44.7	45.2

Table 1. Test case configurations and statistics: u'_1/U_∞ and $L_{11,\infty}/H$ are the incoming turbulence intensity and the normalised integral scale, respectively, measured by the LDV upstream of the dowels; Sc is the Schmidt number of O_2 transport into water; Re_λ is the Taylor micro-scale Reynolds number; Re_T is the turbulent Reynolds number; We is the Weber number; h' and $\overline{S^2}_{PLIF}$ are the r.m.s. variation in the water surface height and the mean-squared free-surface slope measured by PLIF; $\overline{S^2}_{model}$ is the mean-squared slope computed from the model; $\Delta\mathcal{A}$ is the surface area increase relative to a flat surface; u'_{1b}/U_∞ and L_{11}/H are the bulk turbulence intensity and the normalised integral length scale computed from the PIV measurements within the dowel array; k is the gas-transfer velocity.
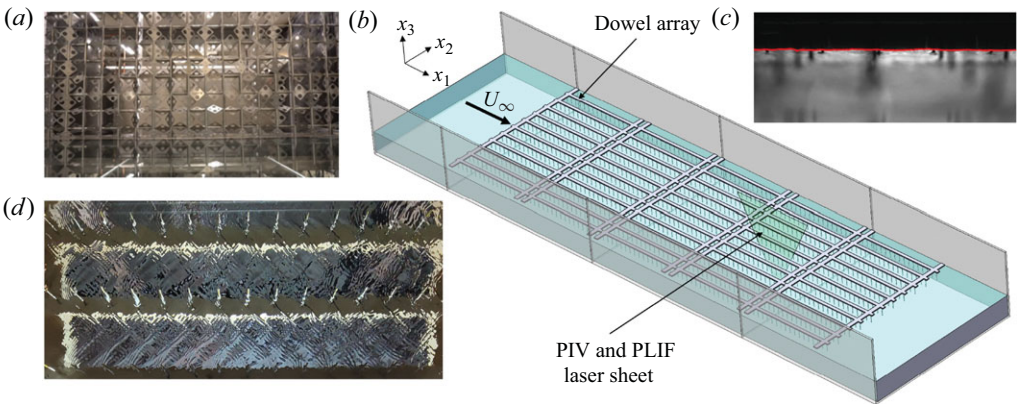

Figure 2. (*a*) The active grid in motion; (*b*) simplified scale schematic of the experimental set-up showing the dowel array and the laser sheet for PIV and PLIF; (*c*) an example PLIF image from case D0, with the surface identified by the red line; (*d*) the surface waves generated by the dowel array as viewed from below the test section.

To characterise the bulk flow, we performed two-component planar particle image velocimetry (PIV) measurements with a LaVision Imager MX 25MP camera. The flow was seeded with 40 μm polystyrene particles, and illumination was provided by a dual-pulse Litron Nano L Nd:YAG laser with a power output of 200 mJ per pulse at 532 nm. The field of view (FOV) was centred at $x_1 = 85M$, was 240 mm wide, and covered the entire depth of the water flow. The instantaneous free-surface height in the FOV plane

is measured by planar laser-induced fluorescence (PLIF) at the same x_1 location as the PIV, using Rhodamine-6G as the fluorescent dye (Buckley & Veron 2017). The dye causes fluorescence in the liquid phase but not in the gas phase when illuminated by the same 532 nm laser used for PIV. Two LaVision Imager sCMOS 4MP cameras were used for PLIF. The PIV images were processed with LaVision DaVis 10 with multiple passes, starting with a 64×64 window and reducing to a final pass window size of 48×48 pixels with 50 % overlap. This results in a final velocity field of 210×210 vectors. The uncertainty in the velocity fields estimated by DaVis is approximately 2 %; uncertainties were calculated based on the PIV correlations (Sciacchitano *et al.* 2015; Wieneke 2015).

From the velocity fields, we calculated the bulk turbulence intensity, u'_{1b}/U_∞, and the streamwise integral length scale L_{11}. We first use Reynolds decomposition to calculate the turbulent velocity fluctuations, *viz.* $u'_1 = u_1 - U_1$, where u_1 is the instantaneous velocity field and U_1 is the mean velocity field. Then, $u'_{1b} = (\int_0^H u'_1 \mathrm{d}x_3)/H$ is the 'bulk' standard deviation of the velocity fluctuations. This is analogous to calculating the bulk velocity from a velocity profile. The integral length scale L_{11} is calculated by first computing the autocorrelation function, B_{uu}, of the velocity fluctuations for $100\,\text{mm} \leqslant x_3 \leqslant 200\,\text{mm}$, *viz.* $B_{uu} = 1 - S_2(r)/(2u'^2_{1b})$, where S_2 is the second-order structure function of the velocity increment and r is the associated spatial increment. This range of x_3 is chosen to be representative of the 'core' flow, avoiding the boundary layer and the near-surface flow. The integral length scale for some cases is larger than our FOV. Thus, we fit an exponential function to the computed autocorrelations such that it asymptotically approaches zero (e.g. Fuchs *et al.* 2022). The integral length scales are then calculated by integrating the fitted function with respect to r. The values for u'_{1b}/U_∞ and L_{11}/H are listed in table 1. It is significant to note that the streamwise length of the exposed surface area for gas transfer is nominally between $10L_{11}$ and $80L_{11}$ depending on the test case, indicating that several turbulent turnovers occur for a single flow through. Moreover, the integral length scales range from approximately one third to twice the water depth, indicating that the large turbulent structures act across a significant portion or the entirety of the water column for all the cases.

From the second-order structure function S_2, we are able to compute the turbulence dissipation rate ϵ, *viz.* $\epsilon = (S_2(r)/(C_n r^{2/3}))^{3/2}$, where $C_n = 2$ is a constant. A sub-range of S_2 that best fits the proportionality relation $S_2(r) \propto r^{2/3}$ is extracted and used for the computation. Then representative mean values of ϵ are calculated for each case. From ϵ, we also estimated the Taylor microscale λ, *viz.* $\lambda^2 = 15\nu u'^2_1/\epsilon$, which then leads to the Taylor micro-scale Reynolds number, $Re_\lambda = u'_1 \lambda/\nu$, listed in table 1. All of these turbulence statistics are computed for the same x_3 range as for L_{11}, namely $100\,\text{mm} \leqslant x_3 \leqslant 200\,\text{mm}$.

Furthermore using the turbulence statistics, we also calculate the turbulence Reynolds number $Re_T = 2u'_{1b}L_{11}/\nu$, the Weber number $We = \rho u'^2_{1b}L_{11}/\sigma$ and the Schmidt number $Sc = \nu/D_{O_2}$. Here, D_{O_2} is the mass diffusivity coefficient of oxygen into water calculated based on the works of Wise & Houghton (1966) and Verhallen *et al.* (1984), and σ is the water surface tension, which is taken to be a nominal value of $0.072\,\text{N m}^{-1}$ based on measurements after the campaign in similar settings using a tensiometer; the measured surface tension of the water in our facility is constant to within 1.5 % of the nominal value. These are also listed in table 1.

The bulk dissolved oxygen concentration (C_b) is measured by an O_2 and pH profiling 0.8 mm diameter extra-fine PreSens Microx 4 optical dipping probe, similar to the one used by Sanjou (2020). The probe is placed at the same streamwise location as the centre of the PIV's FOV ($x_1 = 85M$). The sensing tip penetrates 110 mm below the surface, which has been shown by Nore (2022) to be sufficiently deep into the bulk flow where
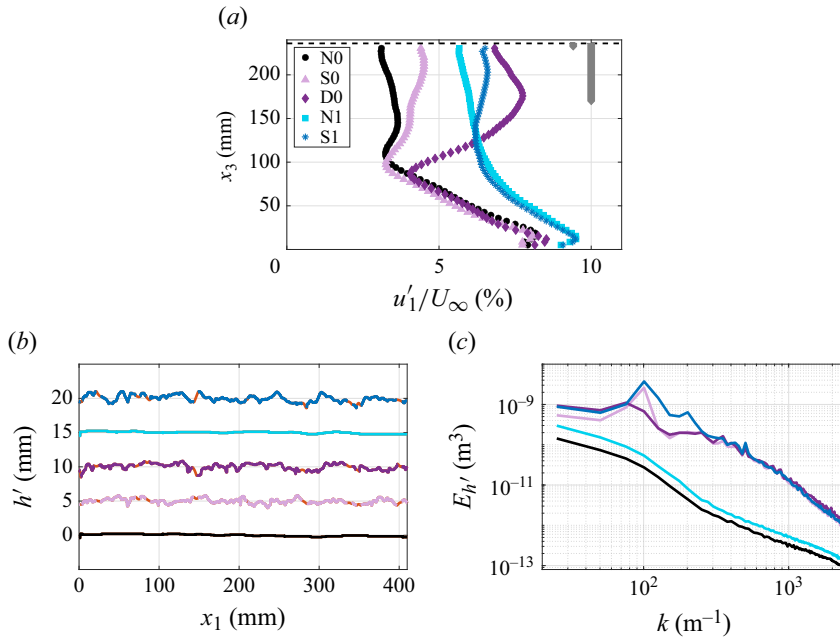
1009 A48-6

Figure 3. (*a*) Turbulence intensity profiles; (*b*) example instantaneous surface topologies extracted from PLIF data, offset by 5 mm between each case for clarity; (*c*) mean spectra of the surface elevation fluctuations. The grey rods in (*a*) represent the dowel penetration depths. The orange segments in (*b*) denote reconstructions of the gaps due to optical blockage by the dowels.

the O_2 concentration no longer changes with depth. Due to the recirculating nature of the water channel, the inflow to the test section is well mixed, resulting in a homogeneous O_2 concentration in the bulk flow, as was also demonstrated by Nore (2022) for this facility. We first removed the original dissolved oxygen in the facility through the addition of sodium sulphite (Na_2SO_3), then oxygen is naturally re-dissolved into the water via the ambient laboratory air (Sanjou 2020). A typical test run takes between 50 and 80 hours for the water to become fully re-saturated with oxygen. The probe samples the bulk oxygen concentration at 0.33 Hz, with pre– and post–calibrations of the probe being performed *in situ* for the zero-concentration and fully saturated reference points before the start and after the end of each run, respectively. Plastic sheets were floated on the water surface outside of the dowel array to ensure that oxygen could only re-aerate through the opening above the array corresponding to where the measurements were performed.

3. Results

We will first show that we are successful in separating the effects of bulk turbulence and surface waves. Figure 3(*a*) presents the turbulence intensity profiles u'_1/U_∞ in x_3. It is evident that the dowels introduce significant velocity fluctuations near the surface. Even at shallow dowel depth, the cumulative effects of the dowel array result in elevated velocity fluctuations ~ 86 mm below the surface, or approximately 10 dowel penetration depths, for both the OFF and the ON grid settings. The deep dowels caused the highest near-surface velocity fluctuations out of all cases, and their effects extend down to ~ 150 mm below the surface. However, we note that the dowels do not affect the turbulence intensities in the bottom boundary layer significantly; their effects are limited to the bulk flow and the near-surface flow. The turbulent velocity fluctuations in the boundary layer are notably higher

when the grid is ON. To account for this, we use the bulk turbulence intensity, u'_{1b}/U_∞, as a quantitative parameter for categorising the cases based on the integrated statistics across the entire flow. From table 1, we can see that cases N0 and S0 have similar turbulence intensities ($\sim 4.5\,\%$), while cases D0, N1 and S1 form another group of similar values ($\sim 6.5\,\%$). In addition, there is a monotonically increasing trend of turbulence intensity from case N0 to S1.

The surface topology can be grouped according to whether the dowels are present or not. Figure 3(b) shows example instantaneous surface profiles extracted from the PLIF measurements for each case, offset by 5 mm each for clarity. Due to optical blockage by the dowels, an autoregressive model is used to reconstruct the gaps in the extracted topology while preserving the statistics of the surface fluctuations. As the PLIF measurements only provide the time-dependent surface topology in x_1, they do not give information in x_2 for calculating the full surface gradient to obtain the mean-squared slope.

The mean-squared free-surface slopes for all cases, $\overline{S^2}_{model}$, listed in table 1, were calculated as follows. Let $\eta(x_1, x_2, t)$ be the free surface, and $\eta_{PLIF}(x_1, t)$ be that measured from PLIF images (figure 2c). We write $\eta = \langle\eta\rangle + \eta'$, with $\langle\cdots\rangle$ the time average, and ascribe $\langle\eta\rangle$ to the standing waves from dowels and η' to turbulence, both due to local variations and unsteadiness in the wave's creation and refraction. The standing wave field $\langle\eta\rangle(x_1, x_2)$ was estimated in the whole plane using linear wave theory of 'fishline waves' (Raphaël & de Gennes 1996) and matching it to $\langle\eta_{PLIF}\rangle$, as detailed in Appendix A. Assuming η' is isotropic on average, $\overline{S^2} = \overline{\langle|\nabla\eta|^2\rangle} = \overline{|\nabla\langle\eta\rangle|^2} + 2\overline{(\partial_1\eta'_{PLIF})^2}$, where an overline denotes the spatial average, $\overline{(\cdots)} = A^{-1}\int_A(\cdots)\mathrm{d}x_1\mathrm{d}x_2$ where A is the full surface area. Without dowels, only the second term is present. Table 1 also lists $\overline{S^2}_{PLIF}$ computed directly from the PLIF measurements as a comparison against $\overline{S^2}_{model}$. In the no-dowel cases N0 and N1, $\overline{S^2}_{model} = 2\overline{S^2}_{PLIF}$ is used. For all the dowel cases, $\overline{S^2}_{model} \approx 1.5\,\overline{S^2}_{PLIF}$. We will subsequently refer to $\overline{S^2}_{model}$ as simply $\overline{S^2}$ for brevity. The mean-squared slope $\overline{S^2}$ provides a simple approximation of the relative change in surface area averaged in time, $\Delta\mathcal{A}$, due to the deformations. Since $|\nabla\eta|^2 \ll 1$, we find by Taylor expansion of the integrand that

$$\Delta\mathcal{A} = \frac{1}{A}\left\langle\int_A\left(\sqrt{1+|\nabla\eta|^2}-1\right)\mathrm{d}x_1\mathrm{d}x_2\right\rangle \approx \frac{1}{A}\left\langle\int_A\frac{1}{2}|\nabla\eta|^2\mathrm{d}x_1\mathrm{d}x_2\right\rangle = \frac{1}{2}\overline{S^2}. \quad (3.1)$$

The value of $\Delta\mathcal{A}$ is also provided in table 1.

Table 1 shows that the mean surface slope becomes an order of magnitude greater when dowel waves are present, i.e. $O(10^{-2})$ without dowels vs. $O(10^{-1})$ with dowels. This puts cases N0 and N1 into one set, and cases S0, D0 and S1 into a second set in terms of surface topology. The mean spatial spectra of the surface profiles shown in figure 3(c), and the root mean square (r.m.s.) of the wave height h' and change in surface area $\Delta\mathcal{A}$ as presented in table 1, are all consistent with the proposed surface topology grouping. The peaks in the spectra in figure 3(c) for cases S0 and S1 correspond to a wavelength of approximately 6 cm, which is the x_1-spacing of the dowels. Case D0 does not have a clearly identifiable peak due to the higher near-surface turbulence polluting any wave coherence.

Figure 4 presents C_b normalised by the saturation concentration C_s as a function of time. Each marker represents a measured average over 15 minutes. Here, C_s is computed from a look-up-table based on the works of Benson & Krause Jr (1980, 1984), with the input being the measured water temperature and the atmospheric pressure for each data point. We can immediately see that cases N0 and S0 exhibit significantly slower C_b recovery rates compared with the other cases. Taking the region between $0.2 \leqslant C_b/C_s \leqslant 0.8$ after
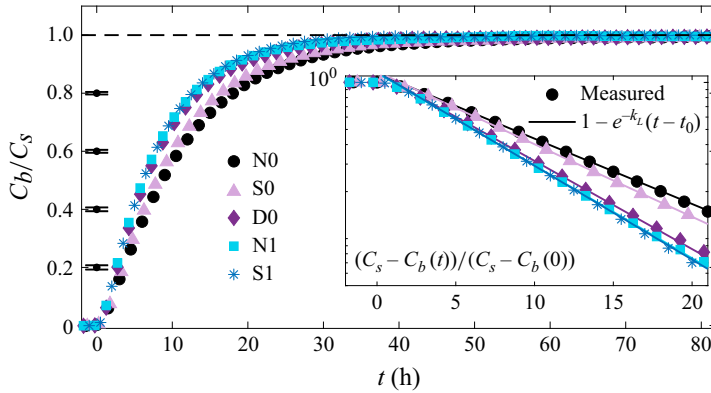
Figure 4. Normalised bulk concentration (C_b) for all test cases. The inset shows the region where C_b/C_s scales with $1 - e^{-k_L(t-t_0)}$. The error bars to the left represent the worst case r.m.s. variations of the 15-minute temporal averaging window at different C_b/C_s values.

the initial C_b uptake for each case, we fit the data points to an exponential function in the form of $1 - e^{-k_L(t-t_0)}$ (e.g. Adler 2022), where k_L and t_0 are fitting parameters.

The gas-transfer velocity is $k = k_L V/A$ (Adler 2022), where V represents the total volume of the water as measured by a flow meter attached to the in-fill pipe, and A denotes the exposed air–water interface surface area beneath the dowel array (9 m^2). The computed values are presented in table 1, and they exhibit a monotonic increase from case N0 to S1 with increasing bulk turbulence intensity. Furthermore, we observe that cases N0 and S0 share similar k values, near 34 cm h^{-1}, while cases D0, N1 and S1 show k clustered near 44 cm h^{-1}; the percentage change in k from N0 to S1 is 45 %. In contrast, the estimated surface area change, $\Delta\mathcal{A} \approx \overline{S^2}/2$, is only $\lesssim 0.7$ % for the no-dowel cases, and $\lesssim 7.7$ %, with the dowels present (see table 1). Bearing in mind that the total rate of gas absorption is proportional to the free-surface area in a quiescent environment, these slight increases in the surface area can neither account for the much larger increase in k for our test conditions, nor do they correlate to the behaviour of k.

4. Discussion

Combining the individual results, we will now discuss the separate effects of bulk turbulence and surface waves on k. First, addressing the surface topology, we have plotted the mean-squared slope $\overline{S^2}$ of the waves against k in figure 5(*a*). Several previous studies have shown that k scales with $\overline{S^2}$ of capillary waves (e.g. Jähne *et al.* 1987; Saylor & Handler 1997). However, we observe no clear trend between $\overline{S^2}$ and k for our cases. Cases D0 and S1 exhibit much higher k than case S0, although they share similar $\overline{S^2}$ values. Similar lack of correlation between $\overline{S^2}$ and k can be observed for the cases without dowels. Moreover, since the relationship between the mean-squared surface gradient and the increase in surface area is linear, $\Delta\mathcal{A} \approx \overline{S^2}/2$, it follows that the gas-transfer rate also does not correlate with surface area. Thus, we conclude that for our test cases, the surface wave topology is not well correlated with the gas-transfer velocity.

In contrast, figure 5(*b*) shows a strong correlation between k and u'_{1b}/U_∞. Nonlinear regression of k in the form of $k = B(\overline{S^2})^m (u'_{1b})^n$, where B, m and n are fitting parameters, shows that $n \approx 0.76$ is two orders of magnitude larger than $m \approx 0.0085$, thereby
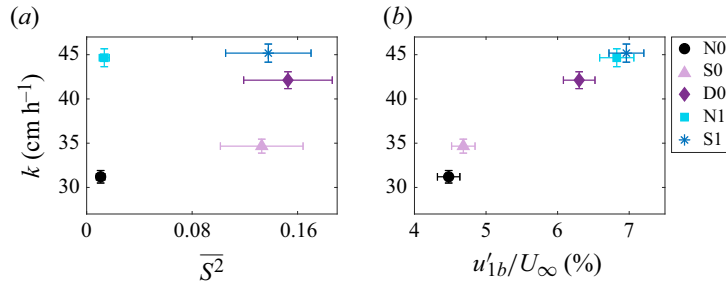
Figure 5. The gas-transfer velocity k vs. (*a*) $\overline{S^2}$ and (*b*) u'_{1b}/U_∞ for all the test cases.

quantitatively confirming the far stronger correlation between k and u'_{1b}/U_∞. To wit, there is strong evidence that k is a linear function of u'_{1b}/U_∞ within our parameter range. A linear fit of figure 5(*b*), with $R^2 \approx 0.98$ (R^2: goodness-of-fit parameter) gives $k(0) \approx 8.9\,\mathrm{cm\,h^{-1}}$, which is close to the range of the experimental results of Liss (1973) for a quiescent laboratory tank ($5.8 - 7.4\,\mathrm{cm\,h^{-1}}$). It is worth noting that k also strongly correlates with Re_λ as listed in table 1. This quantity has the benefit of including both a velocity and a length scale. However, Re_λ is harder to measure outside of the laboratory, and therefore we maintain focus on the fluctuations themselves. Moreover, the turbulence dissipation rate, ϵ, has also been shown to scale with k for field data (e.g. Lamont & Scott 1970; Zappa *et al.* 2007). However, like Re_λ, this quantity is challenging to measure with confidence outside the laboratory.

It is worth noting that the bulk turbulence across the five cases is not created by the same mechanism. In case D0 the turbulence is generated by the wake of the dowels. In cases N1 and S1 the same turbulence level as estimated from u'_{1b}/U_∞ is achieved, but it is produced by the active grid. Nonetheless, the results follow a consistent trend relative to u'_{1b}/U_∞. Identifying why the different spatial mechanisms produce consistent results when considering their bulk statistics should be explored in detail in future studies.

To further illustrate the dominance of bulk turbulence effects over capillary wave effects on k, we examine the Weber number for each case. The values of We for our cases are all near unity, with $We < 1$ for cases N0, S0 and D0. This implies that surface tension is dominant over the sub-surface turbulence in its influence over the flow characteristics, including the surface topology (Brocchini & Peregrine 2001). The fact that the strong correlation we have observed is between k and u'_{1b}/U_∞, not $\overline{S^2}$, despite We being small, indicates the dominance of bulk turbulence over capillary waves. Here, we emphasise that our largest $\overline{S^2}$ (15.3×10^{-2}) exceeds that of Saylor & Handler (1997) (7.4×10^{-2}) by a factor of 2.

Figure 6 shows the relation between $k_{L,660}$, which is k normalised with its associated length scale ($k_L = k\mathcal{L}^{-1}$), and the bulk velocity fluctuations u'_{1b} from Herlina & Jirka (2008), Lacassagne *et al.* (2017), Bullee *et al.* (2024) and the present investigation. The length scale, $\mathcal{L}$, for Herlina & Jirka (2008) and Lacassagne *et al.* (2017) is their water tank depth, while for Bullee *et al.* (2024) and the present work is the ratio V/A. The Schmidt number is used to further normalise k_L, *viz.* $k_{L,660} = k_L(660/Sc)^{-1/2}$ (e.g. Bell *et al.* 2017). The relation between the dimensional velocity fluctuations and $k_{L,660}$ is quite linear, similar to figure 5(*b*). Furthermore, the results from Herlina & Jirka (2008), Lacassagne *et al.* (2017) and the present study fall almost exactly on the same line; the results from Bullee *et al.* (2024) clustering close by. These four studies all had different physical set-ups and different mechanisms for bulk turbulence generation, with Herlina & Jirka (2008) and Lacassagne *et al.* (2017) using an oscillating grid in a quiescent water tank, Bullee
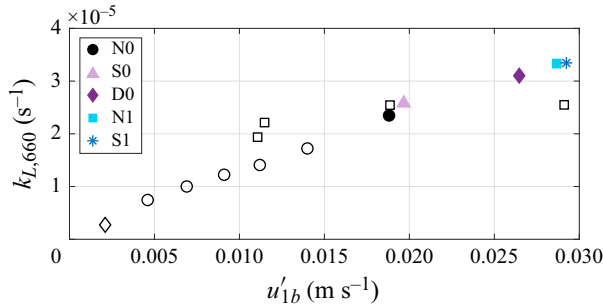
Figure 6. Comparison of the present work with the literature in terms of the turbulent velocity fluctuations u'_1; the open symbols represent: diamond – Lacassagne *et al.* (2017), circle – Herlina & Jirka (2008), square – Bullee *et al.* (2024). The uncertainties in $k_{L,660}$ for the present work are smaller than the marker size and not shown.

et al. (2024) using an active grid in a recirculating water channel and the present work using a combination of active grid turbulence and a dowel array in the same facility. In addition, Lacassagne *et al.* (2017) measured CO_2 while the other studies measured O_2 (hence the need to normalise to $k_{L,660}$). Despite the physical differences, the results from all four studies collapse quite well. This strongly suggests that bulk turbulence is the dominating factor driving k within the non-breaking capillary wave regime that these works investigate.

Our results indicate that laboratory studies using open channel flow with controlled turbulence could be a fruitful avenue for testing gas-transfer parametrisations used to model natural flows. If turbulence and capillary waves are assumed to be equally important to k, creating an experiment which is a convincing analogy to a flow that has been created by a given continuous wind stress would be extremely difficult: to relate one's experiment to a value of u^*, say, one would need to simultaneously recreate key properties of capillary waves and sub-surface turbulence that such a 'hypothetical' wind would have created. Our results show, however, that it is sufficient in the non-breaking regime to tailor the water-side turbulence, whereas capillary surface distortions matter comparatively little. We believe this to be a potentially fructuous avenue for future investigation.

We may note in passing therefore that, while the comparison is imperfect, the clear linear relation between k_L and u'_{1b} is consistent with the relation $k \propto Sc^{-1/2}u^*$ (e.g. Garbe *et al.* 2014) found to hold for wind-driven natural flows and used for modelling the transfer of other, comparable, gases (CO_2 and dimethyl sulphide). Here, u^* is the friction velocity due to the wind stress acting on the surface. Evidence suggests that $u'_3 \sim u^*$ in field studies (D'Asaro 2014), and in our tank we have consistently found $u'_1 \approx 1.2u'_3$. We use only a single Schmidt number, so the scaling with Sc is not tested, but has been well established for nearly flat surfaces (e.g. Magnaudet & Calmet 2006; Esters *et al.* 2017). A number of modifications to this scaling have been developed to account for other environmental factors (e.g. Fairall *et al.* 2011; Deike & Melville 2018), which is important to recognise but it is not clear how to relate our results directly to given the turbulence is in the liquid phase only and parameterisation by air-side quantities does not provide a unique sub-surface flow field. On the other hand, assumption that k scales with the turbulent dissipation rate, ϵ, as has also been employed with some success in ocean models (Lamont & Scott 1970; Zappa *et al.* 2007), can neither be confirmed nor rejected based on our data, although when compared with field measurements they do fall on the same trend, as can be seen in figure 7. A key reason the present results all lie so close to one another in figure 7 is that they are all performed with the same U_∞, while the accumulated field experiments
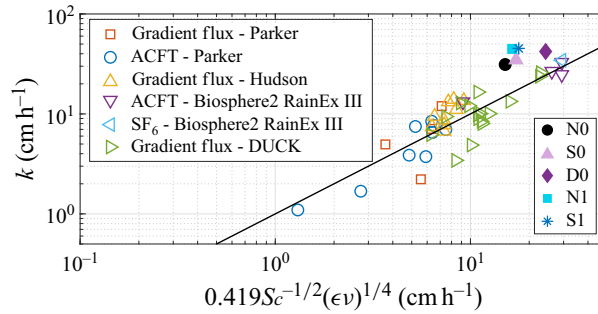
Figure 7. Gas-transfer rate plotted against the small-eddy surface renewal model. The open symbols are from Zappa *et al.* (2007) and the closed symbols are the present work. The uncertainties in k for the present work are smaller than the marker size and not shown.
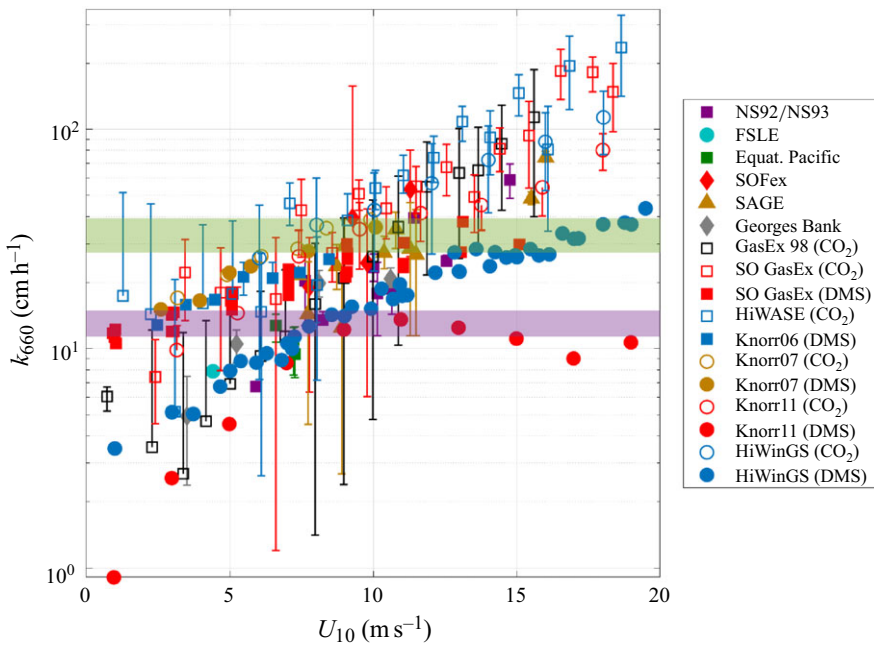

Figure 8. Comparison of the k_{660} range of our present work (denoted by the green shaded region) with select data from the literature. The purple shaded region is the k_{660} range of Bullee *et al.* (2024). The references are: NS92/NS93, Nightingale *et al.* (2000*b*); FSLE, Wanninkhof *et al.* (1997); Equatorial Pacific, Nightingale *et al.* (2000*a*); SOFex, Wanninkhof, Sullivan & Top (2004); SAGE, Ho *et al.* (2006); George Bank, Wanninkhof *et al.* (1993); GasEx 98, McGillis *et al.* (2001); SO GasEx (CO_2), Edson *et al.* (2011); SO GasEX (DMS), Yang *et al.* (2011); HiWASE, Prytherch *et al.* (2010); Knorr06 (DMS), Marandino *et al.* (2009); Knorr07 (CO_2 & DMS), Miller *et al.* (2009); Knorr11 (CO_2 and DMS), Bell *et al.* (2017); HiWinGS (CO_2), Brumer *et al.* (2017); HiWinGS (DMS), Blomquist *et al.* (2017) and Brumer *et al.* (2017). The gas species are ^{3}He/SF_6 unless specified. This figure is built upon the summaries of Wanninkhof *et al.* (2009), Garbe *et al.* (2014) and Deike (2022).

are performed in a variety of conditions. It is thus possible that this scaling reasonably maps differences in k over widely varying conditions, while our results demonstrate how to distinguish the specifics of cases acquired for the same flow rate.

Bearing in mind that the analogy with our study herein and field conditions is far from perfect, it is instructive to explore what might result from mapping the parameter space of the present study onto typical field results accumulated from several sources. In figure 8,

we plot the relation of U_{10} and k for various gas species transfer. For comparison purposes, we normalise our k value by its Schmidt number, *viz.* $k_{660} = k(660/Sc)^{-1/2}$ (e.g. Bell *et al.* 2017). The green shaded band indicates the range of k_{660} from the present study and the purple band is the range from Bullee *et al.* (2024). The range of k_{660} encompassed by the present study has significant overlap with existing field data, especially near $U_{10} \approx$ 10 m s^{-1}. The major benefit of the present investigation is that we can now identify a fluidic cause for the variation within this band, i.e. the sub-surface turbulence intensity can result in variations of the value of k within this range in a predictable fashion. While this is not the entirety of the story in the field, this information on the physics is necessary for the future evolution of predictive modelling of gas transfer in complex systems such as the air–sea interface.

5. Conclusions

The present results demonstrate that the characteristics of the turbulence beneath the surface have a much greater influence on the gas-transfer rate, k, than the presence of non-breaking capillary waves or the water surface deformations more generally. The gas-transfer velocity correlates strongly with turbulence intensity, but is insensitive to the presence or absence of capillaries. The lack of correlation between surface topology and k should not, of course, be extrapolated beyond the regime investigated here, i.e. a weakly distorted surface (classified as 'region 3' in Brocchini & Peregrine 2001). In more violent flows, especially if droplet formation or bubble entrainment occur, the surface can increase locally by orders of magnitude, alongside a host of processes not included in the present investigation, cf. Deike (2022). We acknowledge that past capillary-wave-based studies do show a strong correlation between capillary wave properties and k, which we cannot fully explain. Indeed, in a scenario where there is no sub-surface turbulence but capillary waves are present, one would expect k to scale with the increase in the free-surface area due to the waves, even if such an increase is small. However, there seems to be no definitive evidence in previous studies that the effects of capillary waves were isolated from the sub-surface turbulence or convection. We have observed here that the insertion of dowels, even at a shallow depth, can cause very considerable elevations in velocity fluctuations well into the bulk flow. It is challenging even in laboratory experiments to generate significant and sustained capillary waves without engendering some convective flow. In natural flows it is even more unusual; for instance, wind stress will create both capillary ripples and sub-surface turbulent flow simultaneously. Our findings strongly suggest that, when both sub-surface turbulence and capillary waves are present, the sub-surface turbulence plays a more significant role than surface capillary waves in influencing the dissolution of low-solubility atmospheric gases into water.

Declaration of interests. The authors report no conflict of interest.

Author contributions. L.L., P.A.B., R.J.H. conceived and designed the study; L.L. and P.A.B. conducted the experiments and data analysis; L.L. and S.Å.E. performed the wave modelling; L.L. is the primary author of the manuscript; all authors contributed to the writing and reviewing of the manuscript.

Data availability statement. The data to recreate all the plots in this study are publicly accessible through DataverseNO at https://doi.org/10.18710/IXYMMK.

Appendix A. Theory of capillary waves from a periodic grid of dowels

Capillary-gravity waves in running water created by a thin source, often called the 'fishline problem', has been studied for nearly two centuries (Russell 1844; Thomson (Lord Kelvin) 1871; Rayleigh 1883). A 'fishline' wave pattern is distinguished from that of a 'ship' only by the fact that a source of small size compared with the capillary length scale will primarily create capillary waves, and the latter is conventionally a source of gravity waves; the theory and physics are, however, the same. A lucid account was given by Lamb (1932, § 270–272). To simulate the waves created by a steady wave maker in a running flow, we employ a classical model which is to represent each dowel by a localised patch of increased pressure on the surface, which enters via the dynamic boundary condition (Havelock 1909). The method remains in frequent use, and can yield quantitatively accurate theoretical predictions of experimental ship waves (Smeltzer, Æsøy & Ellingsen 2019). The following theory is similar to Raphaël & de Gennes (1996).

Linear wave theory is assumed and equations of motion are solved in Fourier space, hence all wave quantities are proportional to $\exp[i\kappa_i x_i - i\omega(\boldsymbol{\kappa})t]$ with position $\boldsymbol{x} = (x_1, x_2)$ and wavevector $\boldsymbol{\kappa} = (\kappa_1, \kappa_2)$; we are using Einstein's notation, and $i = 1, 2$ denotes the streamwise and the spanwise directions, respectively. The dispersion relation has two solutions with intrinsic phase velocity parallel and anti-parallel to $\boldsymbol{\kappa}$; for weakly damped waves, it is $\omega_{\pm}(\kappa) = \pm\omega_0(\kappa) + i\gamma$, where $\omega_0(\kappa) = \sqrt{g\kappa + \sigma\kappa^3/\rho}$ and $\kappa = |\boldsymbol{\kappa}|$. Here, g is gravitational acceleration, ρ is water density and σ is the surface tension coefficient. We will assume standard values, $g = 9.81$ m s^{-2}, $\rho \approx 998$ kg m^{-3} and $\sigma \approx 0.072$ N m^{-1}. The viscous damping is $\gamma \approx 2\kappa^2\nu$ for under-damped waves (e.g. Lamb 1932, § 348) with $\nu \approx 1.04 \times 10^{-6}$ m^2 s^{-1} the kinematic viscosity. We may assume $\gamma \ll \omega_0$ for all waves which contribute significantly away from the dowels, and neglect terms of order $(\gamma/\omega_0)^2$.

The surface wave pattern due to an applied pressure $p(\boldsymbol{x})$ on a running stream of velocity U_i is quite generally given by the real part of the expression (Li, Smeltzer & Ellingsen 2019)

$$\eta(\boldsymbol{x}) = \int \frac{\mathrm{d}^2\kappa}{(2\pi)^2} \frac{\kappa\,\tilde{p}(\boldsymbol{\kappa})\mathrm{e}^{i\kappa_i x_i}}{[\omega_+(\kappa) - \kappa_i U_i][\omega_-(\kappa) - \kappa_i U_i]}, \tag{A1}$$

$$\approx -\int \frac{\mathrm{d}^2\kappa}{(2\pi)^2} \frac{\kappa\,\tilde{p}(\boldsymbol{\kappa})\mathrm{e}^{i\kappa_i x_i}}{\omega_0(\kappa)^2 - (\kappa_i U_i)^2 + 2i\kappa_i U_i \gamma}. \tag{A2}$$

We have $\boldsymbol{U} = (U_1, 0)$; $\tilde{p}(\boldsymbol{\kappa}) = \int \mathrm{d}^2x[p(\boldsymbol{x})/\rho]\mathrm{e}^{-i\kappa_i x_i} \equiv \mathcal{F}\{p/\rho\}$ is the Fourier transform of the applied kinematic pressure. The imaginary term in the denominator renders the integral well defined and imposes the appropriate radiation condition.

Let the streamwise and spanwise distance between neighbouring dowels be $a = 60$ mm and $b = 150$ mm, respectively, so the centre of the dowels are at $\boldsymbol{x}_{mn} = (ma, nb)$, where $m, n \in \mathbb{Z}$; the kinematic surface pressure is $p(\boldsymbol{x}) = \sum_{m,n} p_d(\boldsymbol{x} - \boldsymbol{x}_{mn})$, where $p_d(\boldsymbol{x})$ is the pressure patch model of a single dowel at the origin and the sum is over all m and n. Hence

$$\tilde{p}(\boldsymbol{\kappa}) = \frac{1}{\rho}\sum_{m,n} \mathcal{F}\{p(\boldsymbol{x})\} = \frac{1}{\rho}\sum_{m,n} \mathcal{F}\{p_d(\boldsymbol{x} - \boldsymbol{x}_{mn})\} = \tilde{p}_d(\boldsymbol{\kappa})\sum_{m,n} \mathrm{e}^{-i\kappa_i x_{mn,i}}. \tag{A3}$$

For the model pressure patch, we use a circular top hat patch of radius $R = 1.55$ mm, which is the radius of the dowel used in the experiment
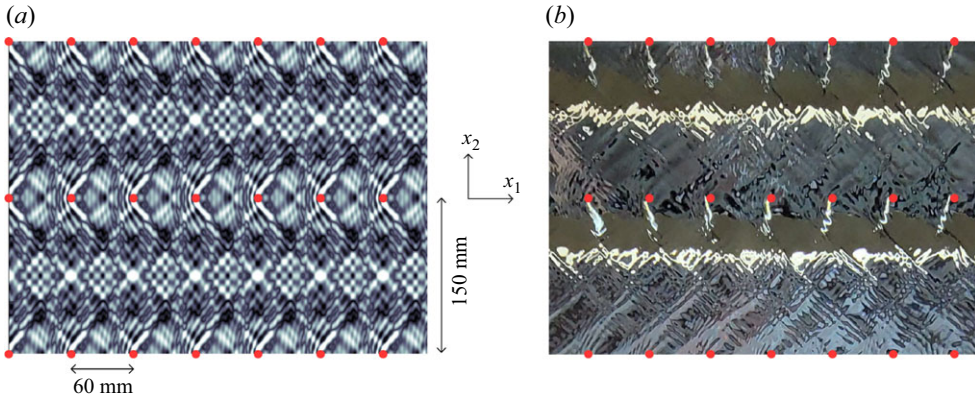
Figure 9. (*a*) Surface elevation calculated from (A2). (*b*) Photo of wave pattern during the experiment. Dowel positions are shown as red spots and are approximate in (*b*). In both panels, the mean flow is from left to right.

$$p_d(\boldsymbol{x}) = \begin{cases} \rho P_0, & |\boldsymbol{x}| \leqslant R, \\ 0 & |\boldsymbol{x}| > R. \end{cases} \tag{A4}$$

An analytical form for $\tilde{p}_d$ can also be found with the expression (A2) written as a discrete-time Fourier transform expression by recognising (A3) as the Dirac comb. However, for our limited purpose it was more convenient to proceed numerically.

We created the kinematic pressure field $p(\boldsymbol{x})$ in space for a domain size of $-4a < x_1 \leqslant 4a$ and $-b < x_2 \leqslant b$. It is then transformed into $\tilde{p}(\boldsymbol{\kappa})$ via a fast Fourier transform (FFT) algorithm and substituted into (A2). Lastly, the model surface topology $\eta(\boldsymbol{x})$ is computed with an inverse FFT of (A2). Figure 9 shows a comparison between the modelled surface elevation and a photo of the wave pattern taken during the experiment. Here, P_0 from (A4) is used as the only tuning parameter of the model to adjust $\eta(\boldsymbol{x})$ along a line $x_2 = b/2$ (i.e. a line midway between dowel rows) to best fit the experimentally measured $\eta_{PLIF}(x_1)$; to wit we minimised the difference in the mean-squared slope $\overline{S^2}$ between the two.

REFERENCES

AARNES, J.R., BABIKER, O.M., XUAN, A., SHEN, L. & ELLINGSEN, S.Å. 2025 Vortex structures under dimples and scars in turbulent free-surface flows. *J. Fluid Mech.* **1007**, A38.

ADLER, K. & COWEN, E.A. 2022 Laboratory investigation of significant gas transfer enhancement via capillary-gravity bow waves. Proceedings of the 8th International Symposium on Gas Transfer at Water Surfaces SOLAS Event Reports, Issue 25, pp. 3–5. SOLAS (Surface Ocean - Lower Atmosphere Study).

ADLER, K.E. 2022 Quantifying and parameterizing air–water gas transfer enhancement via capillary–gravity bow waves and streamwise counter–rotating vortices in environmental and industrial applications. *PhD thesis*, Cornell University, USA.

BABIKER, O.M., BJERKEBÆK, I., XUAN, A., SHEN, L. & ELLINGSEN, S.Å. 2023 Vortex imprints on a free surface as proxy for surface divergence. *J. Fluid Mech.* **964**, R2.

BELL, T.G., LANDWEHR, S., MILLER, S.D., DE BRUYN, W.J., CALLAGHAN, A.H., SCANLON, B., WARD, B., YANG, M.-X. & SALTZMAN, E.S. 2017 Estimation of bubble-mediated air–sea gas exchange from concurrent DMS and CO_2 transfer velocities at intermediate–high wind speeds. *Atmos. Chem. Phys.* **17** (14), 9019–9033.

BENSON, B.B. & KRAUSE D. Jr. 1980 The concentration and isotopic fractionation of gases dissolved in freshwater in equilibrium with the atmosphere. 1. Oxygen. *Limnol. Oceanogr.* **25** (4), 662–671.

BENSON, B.B. & KRAUSE, D. Jr. 1984 The concentration and isotopic fractionation of oxygen dissolved in freshwater and seawater in equilibrium with the atmosphere. *Limnol. Oceanogr* **29** (3), 620–632.

BLOMQUIST, B.W. *et al.* 2017 Wind speed and sea state dependencies of air-sea gas transfer: results from the high wind speed gas exchange study (HiWinGS). *J. Geophy. Res.: Oceans* **122** (10), 8034–8062.

BOCK, E.J., HARA, T., FREW, N.M. & MCGILLIS, W.R. 1999 Relationship between air-sea gas transfer and short wind waves. *J. Geophys. Res.: Oceans* **104** (C11), 25821–25831.

BROCCHINI, M. & PEREGRINE, D.H. 2001 The dynamics of strong turbulence at free surfaces. Part 1. Description. *J. Fluid Mech.* **449**, 225–254.

BRUMER, S.E., ZAPPA, C.J., BLOMQUIST, B.W., FAIRALL, C.W., CIFUENTES-LORENZEN, A., EDSON, J.B., BROOKS, I.M. & HUEBERT, B.J. 2017 Wave-related Reynolds number parameterizations of CO_2 and DMS transfer velocities. *Geophys. Res. Lett.* **44** (19), 9865–9875.

BUCKLEY, M.P. & VERON, F. 2017 Airflow measurements at a wavy air–water interface using PIV and LIF. *Exp. Fluids* **58** (11), 161.

BULLEE, P.A., WEICHERT, S., NORE, A., LI, L., ELLINGSEN, S.Å. & HEARST, R.J. 2024 The influence of water turbulence on surface deformations and the gas transfer rate across an air-water interface. *Exp. Fluids* **65** (9), 132.

COANTIC, M. 1986 A model of gas transfer across air-water interfaces with capillary waves. *J. Geophys. Res. Oceans* **91** (C3), 3925–3943.

COLOMBI, R., ROHDE, N., SCHLÜTER, M. & VON KAMEKE, A. 2022 Coexistence of inverse and direct energy cascades in Faraday waves. *Fluids* **7** (5), 148.

DANCKWERTS, P.V. 1951 Significance of liquid-film coefficients in gas absorption. *Ind. Engng Chem.* **43** (6), 1460–1467.

D'ASARO, E.A. 2014 Turbulence in the upper-ocean mixed layer. *Annu. Rev. Mar. Sci.* **6** (1), 101–115.

DEIKE, L. 2022 Mass transfer at the ocean–atmosphere interface: the role of wave breaking, droplets, and bubbles. *Annu. Rev. Fluid Mech.* **54** (1), 191–224.

DEIKE, L. & MELVILLE, W.K. 2018 Gas transfer by breaking waves. *Geophys. Res. Lett.* **45** (19), 10482–10492.

EDSON, J.B., FAIRALL, C.W., BARITEAU, L., ZAPPA, C.J., CIFUENTES-LORENZEN, A., MCGILLIS, W.R., PEZOA, S., HARE, J.E. & HELMIG, D. 2011 Direct covariance measurement of CO_2 gas transfer velocity during the 2008 Southern ocean gas exchange experiment: wind speed dependency. *J. Geophys. Res. Oceans* **116**, C00F10.

ESTERS, L., LANDWEHR, S., SUTHERLAND, G., BELL, T.G., CHRISTENSEN, K.H., SALTZMAN, E.S., MILLER, S.D. & WARD, B. 2017 Parameterizing air-sea gas transfer velocity with dissipation. *J. Geophys. Res.: Oceans* **122** (4), 3041–3056.

FAIRALL, C.W., YANG, M., BARITEAU, L., EDSON, J.B., HELMIG, D., MCGILLIS, W., PEZOA, S., HARE, J.E., HUEBERT, B. & BLOMQUIST, B. 2011 Implementation of the coupled ocean-atmosphere response experiment flux algorithm with CO_2, dimethyl sulfide, and O_3. *J. Geophys. Res.* **116**, C00F09.

FREW, N.M. *et al.*et al. 2004 Air-sea gas transfer: its dependence on wind stress, small-scale roughness, and surface films. *J. Geophys. Res.: Oceans* **109** (C8), C08S17.

FUCHS, A., KHARCHE, S., PATIL, A., FRIEDRICH, J., WÄCHTER, M. & PEINKE, J. 2022 An open source package to perform basic and advanced statistical analysis of turbulence data and other complex systems. *Phys. Fluids* **34**, 101801.

GARBE, C.S. *et al.* 2014 *Transfer Across the Air-Sea Interface*. Springer.

HAVELOCK, T.H. 1909 The wave-making resistance of ships: a theoretical and practical analysis. *Proc. R. Soc. Lond. A* **82** (554), 276–300.

HEARST, R.J. & LAVOIE, P. 2015 The effect of active grid initial conditions on high Reynolds number turbulence. *Exp. Fluids* **56** (10), 1–20.

HENSTOCK, W.H. & HANRATTY, T.J. 1979 Gas absorption by a liquid layer flowing on the wall of a pipe. *AIChE J.* **25** (1), 122–131.

HERLINA, H. & JIRKA, G.H. 2008 Experiments on gas transfer at the air–water interface induced by oscillating grid turbulence. *J. Fluid Mech.* **594**, 183–208.

HO, D.T., LAW, C.S., SMITH, M.J., SCHLOSSER, P., HARVEY, M. & HILL, P. 2006 Measurements of air-sea gas exchange at high wind speeds in the Southern ocean: implications for global parameterizations. *Geophys. Res. Lett.* **33** (16), L16611.

HORGBY, Å., SEGATTO, P.L., BERTUZZO, E., LAUERWALD, R., LEHNER, B., ULSETH, A.J., VENNEMANN, T.W. & BATTIN, T.J. 2019 Unexpected large evasion fluxes of carbon dioxide from turbulent streams draining the world's mountains. *Nat. Commun.* **10** (1), 4888.

JÄHNE, B., MÜNNICH, K.O., BÖSINGER, R., DUTZI, A., HUBER, W. & LIBNER, P. 1987 On the parameters influencing air-water gas exchange. *J. Geophys. Res. Oceans* **92** (C2), 1937–1949.

JIRKA, G.H., HERLINA, H. & NIEPELT, A. 2010 Gas transfer at the air–water interface: experiments with different turbulence forcing mechanisms. *Exp. Fluids* **49** (1), 319–327.

JOOSS, Y., LI, L., BRACCHI, T. & HEARST, R.J. 2021 Spatial development of a turbulent boundary layer subjected to freestream turbulence. *J. Fluid Mech.* **911**, A4.

KANWISHER, J. 1963*a* Effect of wind on CO2 exchange across the sea surface. *J. Geophys. Res.* **68** (13), 3921–3927.

KANWISHER, J. 1963*b* On the exchange of gases between the atmosphere and the sea. *Deep Sea Res.* **10** (3), 195–207.

KERMANI, A. & SHEN, L. 2009 Surface age of surface renewal in turbulent interfacial transport. *Geophys. Res. Lett.* **36** (10), L10605.

KOMORI, S., NAGAOSA, R. & MURAKAMI, Y. 1993 Turbulence structure and mass transfer across a sheared air–water interface in wind-driven turbulence. *J. Fluid Mech.* **249**, 161–183.

LACASSAGNE, T., EL-HAJEM, M., MORGE, F., SIMOENS, S. & CHAMPAGNE, J.-Y. 2017 Study of gas liquid mass transfer in a grid stirred tank. *Oil & Gas Science and Technology – Revue d'IFP Energies nouvelles* **72** (1), 7.

LAMB, H. 1932 *Hydrodynamics*. 6th edn. Dover Publications.

LAMONT, J.C. & SCOTT, D.S. 1970 An eddy cell model of mass transfer into the surface of a turbulent liquid. *Aiche J.* **16** (4), 513–519.

LI, Y., SMELTZER, B.K. & ELLINGSEN, S.Å. 2019 Transient wave resistance upon a real shear current. *Eur. J. Mech. B: Fluids* **73**, 180–192.

LISS, P.S. 1973 Processes of gas exchange across an air-water interface. *Deep Sea Res.* **20** (3), 221–238.

LONGUET-HIGGINS, M.S. 1992 Capillary rollers and bores. *J Fluid Mech.* **240**, 659–679.

MACINTYRE, F. 1971 Enhancement of gas transfer by interfacial ripples. *Phys. Fluids* **14** (8), 1596–1604.

MAGNAUDET, J. & CALMET, I. 2006 Turbulent mass transfer through a flat shear-free surface. *J. Fluid Mech.* **553**, 155–185.

MAKITA, H. 1991 Realization of a large-scale turbulence field in a small wind tunnel. *Fluid Dyn. Res.* **8** (1-4), 53–64.

MARANDINO, C.A., DE BRUYN, W.J., MILLER, S.D. & SALTZMAN, E.S. 2009 Open ocean DMS air/sea fluxes over the eastern South Pacific ocean. *Atmos. Chem. Phys.* **9** (2), 345–356.

MCCREADY, M.J. & HANRATTY, T.J. 1985 Effect of air shear on gas absorption by a liquid film. *AIChE J.* **31** (12), 2066–2074.

MCGILLIS, W.R., EDSON, J.B., HARE, J.E. & FAIRALL, C.W. 2001 Direct covariance air-sea CO_2 fluxes. *J. Geophys. Res. Oceans* **106** (C8), 16729–16745.

MILLER, S., MARANDINO, C., DE BRUYN, W. & SALTZMAN, E.S. 2009 Air-sea gas exchange of CO_2 and DMS in the North Atlantic by Eddy covariance. *Geophys. Res. Lett.* **36** (15), L15816.

NERNST, W. 1904 Theorie der Reaktionsgeschwindigkeit in heterogenen Systemen. *Zeitschrift für Physikalische Chemie* **47** (1), 52–55.

NIGHTINGALE, P.D., LISS, P.S. & SCHLOSSER, P. 2000*a* Measurements of air-sea gas transfer during an open ocean algal bloom. *Geophys. Res. Lett.* **27** (14), 2117–2120.

NIGHTINGALE, P.D., MALIN, G., LAW, C.S., WATSON, A.J., LISS, P.S., LIDDICOAT, M.I., BOUTIN, J. & UPSTILL-GODDARD, R.C. 2000*b* In situ evaluation of air-sea gas exchange parameterizations using novel conservative and volatile tracers. *Glob. Biogeochem. Cycles* **14** (1), 373–387.

NORE, A. 2022 The effect of turbulence on oxygen uptake of water. Master's thesis, NTNU, Norway.

PÉRINET, N., GUTIÉRREZ, P., URRA, H., MUJICA, N. & GORDILLO, L. 2017 Streaming patterns in Faraday waves. *J. Fluid Mech.* **819**, 285–310.

PRYTHERCH, J., YELLAND, M.J., PASCAL, R.W., MOAT, B.I., SKJELVAN, I. & NEILL, C.C. 2010 Direct measurements of the CO2 flux over the ocean: development of a novel method. *Geophys. Res. Lett.* **37** (3).

RAPHAËL, E. & DE GENNES, P.-G. 1996 Capillary gravity waves caused by a moving disturbance: wave resistance. *Phys. Rev. E* **53** (4), 3448–3455.

RAYLEIGH, L. 1883 The form of standing waves on the surface of running water. *Proc. Lond. Math. Soc.* **1** (1), 69–78.

RUSSELL, J.S. 1844 Report on waves. In *Report of the 14th Meeting of the British Association for the Advancement of Science*, Richard and John E. Taylor.

SANJOU, M. 2020 Local gas transfer rate through the free surface in spatially accelerated open-channel turbulence. *Phys. Fluids* **32** (10), 105103.

SAVELSBERG, R. & VAN DE WATER, W. 2009 Experiments on free-surface turbulence. *J. Fluid Mech.* **619**, 95–125.

SAYLOR, J.R. & HANDLER, R.A. 1997 Gas transport across an air/water interface populated with capillary waves. *Phys. Fluids* **9** (9), 2529–2541.

SCIACCHITANO, A., NEAL, D.R., SMITH, B.L., WARNER, S.O., VLACHOS, P.P., WIENEKE, B. & SCARANO, F. 2015 Collaborative framework for PIV uncertainty quantification: comparative assessment methods. *Meas. Sci. Technol.* **26** (7), 074004.

SMELTZER, B.K., ÆSØY, E. & ELLINGSEN, S.Å. 2019 Observation of surface wave patterns modified by sub-surface shear currents. *J. Fluid Mech.* **873**, 508–530.

SMELTZER, B.K., RØMCKE, O., HEARST, R.J. & ELLINGSEN, S.Å. 2023 Experimental study of the mutual interactions between waves and tailored turbulence. *J. Fluid Mech.* **962**, R1.

SZERI, A.J. 1997 Capillary waves and air-sea gas transfer. *J. Fluid Mech.* **332**, 341–358.

THOMSON (LORD KELVIN), W. 1871 Ripples and waves. *Nature* **5** (105), 1–2.

VARIANO, E.A. & COWEN, E.A. 2013 Turbulent transport of a high-Schmidt-number scalar near an air–water interface. *J. Fluid Mech.* **731**, 259–287.

VERHALLEN, P.T.H.M., OOMEN, L.J.P., VD ELSEN, A.J.J.M., KRUGER, J. & FORTUIN, J.M.H. 1984 The diffusion coefficients of helium, hydrogen, oxygen and nitrogen in water determined from the permeability of a stagnant liquid layer in the quasi-steady state. *Chem. Engng Sci.* **39** (11), 1535–1541.

WANNINKHOF, R., ASHER, W., WEPPERNIG, R., CHEN, H., SCHLOSSER, P., LANGDON, C. & SAMBROTTO, R. 1993 Gas transfer experiment on Georges bank using two volatile deliberate tracers. *J. Geophys. Res. Oceans* **98** (C11), 20237–20248.

WANNINKHOF, R., ASHER, W.E., HO, D.T., SWEENEY, C. & MCGILLIS, W.R. 2009 Advances in quantifying air-sea gas exchange and environmental forcing. *Annu. Rev. Mar. Sci.* **1** (1), 213–244.

WANNINKHOF, R. *et al.* 1997 Gas exchange, dispersion, and biological productivity on the west Florida shelf: results from a Lagrangian tracer study. *Geophys. Res. Lett.* **24** (14), 1767–1770.

WANNINKHOF, R., SULLIVAN, K.F. & TOP, Z. 2004 Air-sea gas transfer in the Southern Ocean. *J. Geophys. Res. Oceans* **109** (C8), C08S17.

WIENEKE, B. 2015 PIV uncertainty quantification from correlation statistics. *Meas. Sci. Technol.* **26** (7), 074002.

WISE, D.L. & HOUGHTON, G. 1966 The diffusion coefficients of ten slightly soluble gases in water at 10-60 °C. *Chem. Engng Sci.* **21** (11), 999–1010.

WOOLF, D.K. *et al.* 2019 Key uncertainties in the recent air-sea flux of CO_2. *Glob. Biogeochem. Cycles* **33** (12), 1548–1563.

YANG, M., BLOMQUIST, B.W., FAIRALL, C.W., ARCHER, S.D. & HUEBERT, B.J. 2011 Air-sea exchange of dimethylsulfide in the Southern Ocean: measurements from SO GasEx compared to temperate and tropical regions. *J. Geophys. Res. Oceans* **116** (C4), C00F05.

ZAPPA, C.J., MCGILLIS, W.R., RAYMOND, P.A., EDSON, J.B., HINTSA, E.J., ZEMMELINK, H.J., DACEY, J.W.H. & HO, D.T. 2007 Environmental turbulent mixing controls on air-water gas exchange in marine and aquatic systems. *Geophys. Res. Lett.* **34** (10), L10601.